Analysis of Axisymmetric Waveguide Components by a Multi-Domain Spectral Method

Analysis of Axisymmetric Waveguide Components by a Multi-Domain Spectral Method

Alberto Tibaldi, *Graduate Student Member, IEEE,* Giuseppe Addamo, Oscar Antonio Peverini, *Member, IEEE,* Renato Orta, *Senior Member, IEEE,* Giuseppe Virone and Riccardo Tascone, *Member, IEEE*

***Abstract*—A novel full-wave method aimed at analyzing axisymmetric waveguide devices is introduced in this paper. The method is based on the application of the equivalence theorem in order to decouple the outer and inner electromagnetic problems. The former refers to the access waveguides, the latter to the complex shape structure inside the device, which is modeled as a boundary value problem and solved by means of a multi-domain spectral method. Detailed comparisons with other simulation codes are reported for two benchmark structures and for a complex axisymmetric waveguide component.**

***Index Terms*—Axisymmetric waveguide components, spectral methods, mortar-matching, horn antennas.**

I. Introduction

WAVEGUIDE components are widely used as building blocks for complex radio-frequency systems, especially in high-frequency and high-power applications, such as satellite telecommunication payloads. Therefore, the development of tools aimed at performing accurate and fast analyses oriented to the computer-aided design (CAD) of these devices still plays a major role in the electromagnetic research. In this context, the present paper focuses on the analysis of waveguide structures exhibiting axial symmetry, such as the simple junction between a circular and a conical waveguide shown in Fig. 1. Although in regions 1 and 3 the electromagnetic field can be represented by means of circular and conical waveguide modes respectively, no modal representation of the field in region 2 is available [1]. Hence, the application of the mode-matching technique (MMT) to this discontinuity is not straightforward. A solution commonly adopted to overcome this problem is based on the introduction of a staircase approximation of the tapered profile. The discretized geometry is, then, analyzed as a cascade of waveguide steps, where each step is characterized by its generalized scattering matrix (GSM). Each GSM is obtained by applying either the mode-matching technique or the method of moments [2], [3], [4]. However, this technique is not particularly suitable for the analysis of complex-shape structures, *e.g.*, choked mode converters used in compact corrugated horn antennas [5], [6], [7].

A finite-element formulation (FEM) of scattering problems involving penetrable bodies of revolution has been introduced in the late '70s [8]. Recently, another FEM-based formulation has been applied to the development of a CAD tool for radiating structures [9].

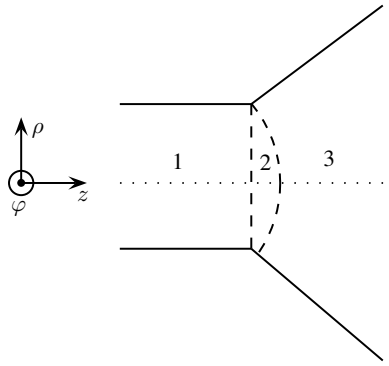

Fig. 1. Longitudinal section of a junction between a circular and a conical waveguide. The dotted line is the longitudinal axis, whereas the dashed lines denote the waveguide ports for the regions 1 and 3.

Among all the techniques that can be used to analyze waveguide devices, spectral methods are very interesting candidates. These schemes have been already applied to several engineering models based on partial differential equations (PDEs), especially in structural mechanics and in computational fluid dynamics [10], [11]. They derive from the method of weighted residuals, where a set of basis functions is used to approximate the solution of the PDE and a weak formulation is used to minimize the error in the expansion. Unlike in FEMs, where the domain is divided into several small elements and low-order local functions are used to expand the solution and to test the equations, in spectral methods both the expansion and test functions are chosen to be infinitely differentiable entire-domain functions. Multi-domain spectral methods enable the application of these schemes to complex regions, which cannot be mapped to a simple reference domain [12]. Owing to their flexibility in the description of complex geometries, these methods have been recently applied to several electromagnetic problems in both frequency and time domains [13], [14], [15]. In [16], the authors have presented a multi-domain spectral method for the solution of the scalar Helmholtz equation relevant to the analysis of E-plane and H-plane devices in rectangular waveguide. This is based on the numerical synthesis of a set of orthonormal entire-domain boundary-adapted functions through the application of the singular value decomposition and the mortar-matching technique [12].

Starting from [16], this paper reports a novel analysis

A. Tibaldi and R. Orta are with the Department of Electronics and Telecommunications, Politecnico di Torino, Torino, 10129 Italy (e-mail: alberto.tibaldi@polito.it).

O. A. Peverini, G. Addamo, G. Virone and R. Tascone are with the Consiglio Nazionale delle Ricerche (CNR), Istituto di Elettronica e di Ingegneria dell'Informazione e delle Telecomunicazioni (IEIIT), 10129 Turin, Italy.

Manuscript received July 12, 2014; revised xxxxx xx, xxxx.

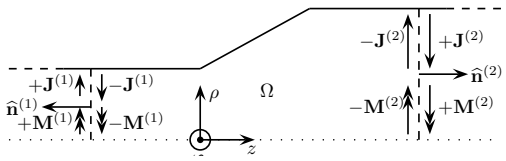

Fig. 2. Reference structure consisting in the transition between two circular waveguides. $\mathbf{J}^{(k)}$ and $\mathbf{M}^{(k)}$ denote the equivalent electric and magnetic currents introduced on both sides of the surface $\gamma_{\mathrm{wg}}^{(k)}$ (vertical dashed lines) at the k-th access port.

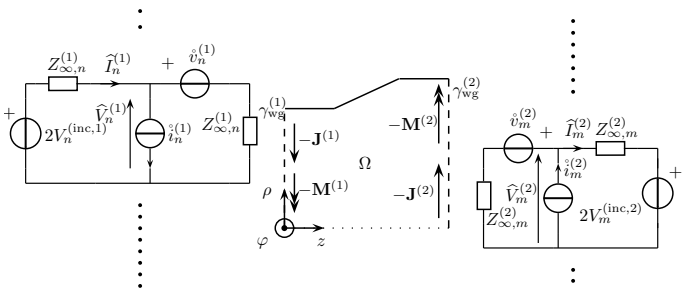

Fig. 3. Hybrid equivalent multi-modal circuit of the waveguide structure shown in Fig. 2, where only one equivalent modal circuit is shown for each access waveguide.

technique of axisymmetric waveguide structures. In Subsection II-A, the electromagnetic problem is formulated by means of the equivalence theorem, which is used to decouple the outer and inner sub-problems. The former refers to the canonical access waveguides for which the modal basis representation is available, whereas the latter is defined on the complex-shape region inside the device, where the boundary value problem is solved by means of a multi-domain spectral method, *i.e.*, the Mortar-Element Method (MEM) (Subsection II-B). Then, the inner and outer problems are coupled by enforcing the continuity conditions of the tangential fields at the access ports (Subsection II-C). Section III reports the validation of the present method by comparison with other numerical techniques for two benchmark cases and for a choked mode converter.

II. Theory

The present method is applicable to structures exhibiting axial symmetry and containing any type of access waveguide ports, *e.g.*, circular, coaxial or conical waveguides. For the sake of clarity and without loss of generality, the method is here described by considering the reference structure shown in Fig. 2 consisting in a transition between two circular waveguides.

A. Decomposition of the problem

The electromagnetic problem is decomposed into a sub-problem defined on the inner region Ω of the structure (with boundary γ) and several sub-problems relative to the N_{Ports} access waveguides. In each waveguide, the transverse fields are represented in the modal basis:

$$\mathbf{E}_{\mathrm{t}}^{(k)} = \sum_{n=1}^{N_{\mathrm{m}}^{(k)}} V_n^{(k)}\, \mathbf{e}_n^{(k)} \tag{1}$$

$$\mathbf{H}_{\mathrm{t}}^{(k)} = \sum_{n=1}^{N_{\mathrm{m}}^{(k)}} I_n^{(k)}\, \mathbf{h}_n^{(k)}, \tag{2}$$

where $N_{\mathrm{m}}^{(k)}$ is the number of modes chosen at the k-th waveguide port.

The method is based on the solution of two matrix equations: the first one is derived from the Maxwell's curl equations defined on the domain Ω, and the second one is related to the continuity of the tangential electric and magnetic fields at the access ports $\gamma_{\mathrm{wg}}^{(k)}$. Let $\widehat{\mathbf{E}}_{\mathrm{t}}^{(k)}$, $\widehat{\mathbf{H}}_{\mathrm{t}}^{(k)}$, ($\widetilde{\mathbf{E}}_{\mathrm{t}}^{(k)}$, $\widetilde{\mathbf{H}}_{\mathrm{t}}^{(k)}$) be the transverse electric and magnetic fields on the outer (inner) side of $\gamma_{\mathrm{wg}}^{(k)}$. The decomposition of the original problem into sub-problems is carried out by applying the equivalence theorem. Accordingly, a couple of oppositely directed electric and magnetic current densities are introduced on the two sides of $\gamma_{\mathrm{wg}}^{(k)}$ (see Fig. 2):

$$\mathbf{J}^{(k)} = \hat{\mathbf{n}}^{(k)} \times \widehat{\mathbf{H}}_{\mathrm{t}}^{(k)}, \qquad \mathbf{M}^{(k)} = \widehat{\mathbf{E}}_{\mathrm{t}}^{(k)} \times \hat{\mathbf{n}}^{(k)}, \tag{3}$$

where $\hat{\mathbf{n}}^{(k)}$ is the external normal to $\gamma_{\mathrm{wg}}^{(k)}$. As well known, the equivalent currents $+\mathbf{J}^{(k)}$ and $+\mathbf{M}^{(k)}$ give rise to $\widehat{\mathbf{E}}_{\mathrm{t}}^{(k)}$, $\widehat{\mathbf{H}}_{\mathrm{t}}^{(k)}$ and to a null field inside the region Ω, allowing the choice of an arbitrary waveguide termination. For what follows, it is convenient to choose a matched load. Correspondingly, $-\mathbf{J}^{(k)}$ and $-\mathbf{M}^{(k)}$ produce $\widetilde{\mathbf{E}}_{\mathrm{t}}^{(k)}$, $\widetilde{\mathbf{H}}_{\mathrm{t}}^{(k)}$.

The equivalent currents can be conveniently represented in the waveguide modal basis:

$$\mathbf{J}^{(\mathrm{k})} = \sum_{n=1}^{N_{\mathrm{m}}^{(k)}} \mathring{i}_n^{(k)} \mathbf{e}_n^{(k)}, \qquad \mathbf{M}^{(\mathrm{k})} = \sum_{n=1}^{N_{\mathrm{m}}^{(k)}} \mathring{v}_n^{(k)} \mathbf{h}_n^{(k)}. \tag{4}$$

By choosing $\gamma_{\mathrm{wg}}^{(k)}$ far enough from abrupt discontinuities inside the device, a small number of modes $N_{\mathrm{m}}^{(k)}$ is necessary. The coefficients $\mathring{i}_n^{(k)}$ and $\mathring{v}_n^{(k)}$ have the circuit interpretation of current and voltage generators on the modal lines [17, Chap. 2]. Accordingly, a hybrid circuit can be associated to the waveguide device, where the electromagnetic problem in each access waveguide is represented by an equivalent multi-modal circuit. Fig. 3 shows the circuit associated to the reference structure of Fig. 2, where only one equivalent modal circuit is shown for each access waveguide. Here, $Z_{\infty,n}^{(k)}$ is the modal characteristic impedance and $V_n^{(k,\mathrm{inc})}$ is the modal projection of the incident field at the k-th waveguide port. As detailed in the following, the unknown current and voltage generators are found by solving the relevant boundary value problem and by enforcing the continuity of the fields radiated by the corresponding equivalent currents in the different sub-regions.

B. Boundary Value Problem in the inner domain

The boundary value problem defined in the inner region Ω of the structure is derived from the curl Maxwell's equations in absence of sources, written in cylindrical coordinates. Indeed, the only sources in this problem are the equivalent

surface currents defined on the access ports and their effect is accounted for by means of non-homogeneous boundary conditions. As in the 2-D analysis of E/H-plane components [16], the electromagnetic problem in axisymmetric devices is conveniently formulated in terms of the field components directed along the invariance direction of the structure, which in this case are E_φ and H_φ. Therefore, the relevant PDEs to be solved are the φ-components of the curl Maxwell's equations:

$$\frac{\partial H_\rho}{\partial z} - \frac{\partial H_z}{\partial \rho} = \mathrm{j}k_0 Y_0 E_\varphi \tag{5}$$

$$\frac{\partial E_\rho}{\partial z} - \frac{\partial E_z}{\partial \rho} = -\mathrm{j}k_0 Z_0 H_\varphi, \tag{6}$$

where the other field components are expressed in terms of E_φ and H_φ as:

$$\begin{aligned}
E_\rho &= -\frac{\mathrm{j}}{m^2 - k_0^2\rho^2}\left(m\frac{\partial(\rho E_\varphi)}{\partial \rho} + k_0 Z_0 \rho^2 \frac{\partial H_\varphi}{\partial z}\right)\\
H_\rho &= -\frac{\mathrm{j}}{m^2 - k_0^2\rho^2}\left(-k_0 Y_0 \rho^2 \frac{\partial E_\varphi}{\partial z} + m\frac{\partial(\rho H_\varphi)}{\partial \rho}\right)\\
E_z &= -\frac{\mathrm{j}}{m^2 - k_0^2\rho^2}\left(m\rho\frac{\partial E_\varphi}{\partial z} - k_0 Z_0 \rho \frac{\partial(\rho H_\varphi)}{\partial \rho}\right)\\
H_z &= -\frac{\mathrm{j}}{m^2 - k_0^2\rho^2}\left(k_0 Y_0 \rho\frac{\partial(\rho E_\varphi)}{\partial \rho} + m\rho\frac{\partial H_\varphi}{\partial z}\right).
\end{aligned} \tag{7}$$

In these equations, k_0 is the free-space wavenumber, Z_0 is the free-space impedance and $Y_0 = Z_0^{-1}$. Moreover, the angular derivative has been substituted by $\mathrm{j}m$, being m the index of the incident cylindrical harmonic $\mathrm{e}^{\mathrm{j}m\varphi}$. Unless $m = 0$, these components depend on both E_φ and H_φ and, hence, the boundary value problem is vectorial. It has to be noted that the singularity in $\rho = m/k_0$ appearing in the right-hand sides of (7) is removable, since these expressions represent regular functions. Equations (5)-(7) are supplemented with the boundary conditions on the PEC boundary of the structure γ_{PEC}

$$\begin{cases} E_\varphi = 0 & (z,\rho) \in \gamma_{\mathrm{PEC}} \\ \mathbf{E}_{\mathrm{t}}^{(\varphi)} \cdot \hat{\mathbf{s}} = 0 & (z,\rho) \in \gamma_{\mathrm{PEC}}, \end{cases} \tag{8}$$

where $\mathbf{E}_{\mathrm{t}}^{(\varphi)}$ is the electric field in the (z,ρ) plane and $\hat{\mathbf{s}}$ is the tangent unit vector of γ_{PEC}.

In the present mortar-element method, the unknown fields E_φ and H_φ inside the component are represented as linear combinations of entire-domain basis functions defined on the region Ω:

$$\begin{aligned}
E_\varphi &= \sum_{c=1}^{N_{\mathrm{fun}}^{(\mathrm{e})}} c_c^{(\mathrm{e})} u_c^{(\mathrm{e})}(z,\rho)\\
H_\varphi &= \sum_{c=1}^{N_{\mathrm{fun}}^{(\mathrm{h})}} c_c^{(\mathrm{h})} u_c^{(\mathrm{h})}(z,\rho).
\end{aligned} \tag{9}$$

The basis functions $u_c^{(\mathrm{h})}$ belong to the space $V^{(\mathrm{h})}$ of continuous functions with integrable derivatives, whereas $u_c^{(\mathrm{e})}$ belong to the sub-space $V^{(\mathrm{e})} \subset V^{(\mathrm{h})}$, that includes only functions vanishing on γ_{PEC}. This choice is related to the fact that the Dirichlet condition on E_φ is an essential boundary condition and, hence, it has to be explicitly enforced. On the contrary, the condition on $\mathbf{E}_{\mathrm{t}}$ is of natural type and, consequently, it is enforced in the weak formulation without specializing the functions used to represent H_φ [19, Chap. 3]. These sets of entire-domain basis functions are numerically synthesized by decomposing the region Ω in sub-domains that are mapped to a square parent domain (u,v) through blending mappings. Then, a set of local basis functions is defined in the parent domain for each patch. These functions are specialized to satisfy the essential boundary conditions and to keep into account the singular behavior of the electromagnetic field in presence of sharp edges [18]. Finally, the sets of local functions defined on distinct patches are glued at the common edges of adjacent patches by means of the mortar-matching method. Additional details about the numerical synthesis of the basis functions are reported in [16].

In order to derive the weak formulation of the present boundary value problem, (5) is tested on functions $v_r^{(\mathrm{e})} \in V^{(\mathrm{e})}$, while (6) is tested on $v_r^{(\mathrm{h})} \in V^{(\mathrm{h})}$. By applying integration by parts, the following expressions are derived:

$$(\mathrm{LHS})^{(\mathrm{e})} = (\mathrm{RHS})^{(\mathrm{e})} \qquad \forall r = 1 \ldots N_{\mathrm{fun}}^{(\mathrm{e})} \tag{10}$$

$$(\mathrm{LHS})^{(\mathrm{h})} = (\mathrm{RHS})^{(\mathrm{h})} \qquad \forall r = 1 \ldots N_{\mathrm{fun}}^{(\mathrm{h})}, \tag{11}$$

where:

$$\begin{aligned}
(\mathrm{LHS})^{(\mathrm{e})} = {} & \mathrm{j}k_0 Y_0 \iint_\Omega E_\varphi v_r^{(\mathrm{e})*} \mathrm{d}\rho\mathrm{d}z + \\
& + \iint_\Omega \left[H_\rho \frac{\partial v_r^{(\mathrm{e})*}}{\partial z} - H_z \frac{\partial v_r^{(\mathrm{e})*}}{\partial \rho}\right] \mathrm{d}\rho\mathrm{d}z
\end{aligned} \tag{12}$$

$$(\mathrm{RHS})^{(\mathrm{e})} = \oint_\gamma (\mathbf{H}_{\mathrm{t}}^{(\varphi)} v_r^{(\mathrm{e})*}) \cdot \mathrm{d}\mathbf{s} \tag{13}$$

$$\begin{aligned}
(\mathrm{LHS})^{(\mathrm{h})} = {} & -\mathrm{j}k_0 Z_0 \iint_\Omega H_\varphi v_r^{(\mathrm{h})*} \mathrm{d}\rho\mathrm{d}z + \\
& + \iint_\Omega \left[E_\rho \frac{\partial v_r^{(\mathrm{h})*}}{\partial z} - E_z \frac{\partial v_r^{(\mathrm{h})*}}{\partial \rho}\right] \mathrm{d}\rho\mathrm{d}z
\end{aligned} \tag{14}$$

$$(\mathrm{RHS})^{(\mathrm{h})} = \oint_\gamma (\mathbf{E}_{\mathrm{t}}^{(\varphi)} v_r^{(\mathrm{h})*}) \cdot \mathrm{d}\mathbf{s}, \tag{15}$$

where γ is the boundary of Ω. As it can be inferred from (7), the contribution of the axis $\rho = 0$ to the line integrals (13) and (15) is zero. Also the contribution of γ_{PEC} to (13) vanishes, since test functions belonging to $V^{(\mathrm{e})}$ are involved. The contribution of γ_{PEC} to the line integral (15) is set to zero in order to enforce the condition $\mathbf{E}_{\mathrm{t}}^{(\varphi)} \cdot \mathbf{s} = 0$ in the weak formulation. For these reasons, the only non-vanishing contributions to the line integrals (13) and (15) come from the equivalent currents defined on the access ports. Noting that in these regions $\mathbf{E}_{\mathrm{t}}^{(\varphi)} \cdot \mathrm{d}\mathbf{s} = \widetilde{\mathbf{E}}_{\mathrm{t}}^{(k)} \cdot \mathrm{d}\mathbf{s}$ and $\mathbf{H}_{\mathrm{t}}^{(\varphi)} \cdot \mathrm{d}\mathbf{s} = \widetilde{\mathbf{H}}_{\mathrm{t}}^{(k)} \cdot \mathrm{d}\mathbf{s}$, the following quantities can be defined:

$$\begin{aligned}
b_r^{(\mathrm{e},k)} \triangleq {} & \int_{\gamma_{\mathrm{wg}}^{(k)}} (\widetilde{\mathbf{H}}_{\mathrm{t}}^{(k)} v_r^{(\mathrm{e})*}) \cdot \mathrm{d}\mathbf{s} = \\
& \int_{\gamma_{\mathrm{wg}}^{(k)}} (\mathbf{J}^{(k)} \times \hat{\mathbf{n}}^{(k)} v_r^{(\mathrm{e})*}) \cdot \mathrm{d}\mathbf{s} \\
b_r^{(\mathrm{h},k)} \triangleq {} & \int_{\gamma_{\mathrm{wg}}^{(k)}} (\widetilde{\mathbf{E}}_{\mathrm{t}}^{(k)} v_r^{(\mathrm{h})*}) \cdot \mathrm{d}\mathbf{s} = \\
& \int_{\gamma_{\mathrm{wg}}^{(k)}} (\hat{\mathbf{n}}^{(k)} \times \mathbf{M}^{(k)} v_r^{(\mathrm{h})*}) \cdot \mathrm{d}\mathbf{s},
\end{aligned} \tag{16}$$

where (3) and the field continuity have been exploited. With reference to (10) and (11), by expressing all the field components in terms of E_φ and H_φ through (7) and by substituting the basis function expansions (9) of E_φ and H_φ, the following linear system is derived:

$$\begin{cases} \mathbf{A}^{(\mathrm{e,e})} \cdot \mathbf{c}^{(\mathrm{e})} + \mathbf{A}^{(\mathrm{e,h})} \cdot \mathbf{c}^{(\mathrm{h})} = \displaystyle\sum_{k=1}^{N_{\mathrm{Ports}}} \mathbf{b}^{(\mathrm{e},k)} \\ \mathbf{A}^{(\mathrm{h,e})} \cdot \mathbf{c}^{(\mathrm{e})} + \mathbf{A}^{(\mathrm{h,h})} \cdot \mathbf{c}^{(\mathrm{h})} = \displaystyle\sum_{k=1}^{N_{\mathrm{Ports}}} \mathbf{b}^{(\mathrm{h},k)}, \end{cases} \tag{17}$$

being $\mathbf{c}^{(\mathrm{e})}$ and $\mathbf{c}^{(\mathrm{h})}$ the vectors containing the expansion coefficients defined in (9). The first equation comes from the projections on the test functions $v_r^{(\mathrm{e})}$ of the terms of (12) related to E_φ ($\mathbf{A}^{(\mathrm{e,e})}$) and to H_φ ($\mathbf{A}^{(\mathrm{e,h})}$). Likewise, the second equation is related to the projection of the terms of (14) on $v_r^{(\mathrm{h})}$. The vectors $\mathbf{b}^{(\mathrm{e},k)}$ and $\mathbf{b}^{(\mathrm{h},k)}$ contain the integrals at the access ports defined in (16). By exploiting (4), these vectors are expressed in terms of the modal generator vectors $\mathring{\mathbf{i}}^{(k)}$ and $\mathring{\mathbf{v}}^{(k)}$ as:

$$\begin{aligned} \mathbf{b}^{(\mathrm{e},k)} &= \mathbf{B}^{(\mathrm{e},k)} \cdot \mathring{\mathbf{i}}^{(k)} \\ \mathbf{b}^{(\mathrm{h},k)} &= \mathbf{B}^{(\mathrm{h},k)} \cdot \mathring{\mathbf{v}}^{(k)}. \end{aligned} \tag{18}$$

Finally, substitution of (18) in (17) yields the linear system:

$$\mathbf{A} \cdot \mathbf{c} = \mathbf{B} \cdot \mathbf{x}, \tag{19}$$

where

$$\mathbf{c} = \begin{bmatrix} \mathbf{c}^{(\mathrm{e})} \\ \mathbf{c}^{(\mathrm{h})} \end{bmatrix}, \qquad \mathbf{x} = \begin{bmatrix} \mathring{\mathbf{i}}^{(1)} \\ \mathring{\mathbf{v}}^{(1)} \\ \vdots \\ \mathring{\mathbf{i}}^{(k)} \\ \mathring{\mathbf{v}}^{(k)} \\ \vdots \end{bmatrix}. \tag{20}$$

The expressions of the matrix elements of (19) for the two-port circular waveguide device shown in Fig. 2 are reported in Appendix A. It is to be remarked that (19) establishes a relationship between the equivalent currents defined on each waveguide port and the MEM expansion coefficients of the fields E_φ and H_φ inside the structure. Hence, solving (19) with respect to $\mathbf{x}$,

$$\mathbf{c} = \mathbf{G} \cdot \mathbf{x} = \mathbf{A}^{-1} \cdot \mathbf{B} \cdot \mathbf{x}, \tag{21}$$

a representation of the Green's function of Ω is obtained.

As evident from (7), the functions involved in the calculation of the matrix elements can contain a singularity in $\rho = m/k_0$. This problem has been tackled by means of the singularity-subtraction scheme reported in Appendix B.

C. Continuity conditions

In order to solve the electromagnetic problem, the inner and outer sub-problems have to be coupled through the continuity conditions at each waveguide port. This is enforced in weak form by projection on the waveguide mode functions:

$$\begin{cases} \langle \widetilde{\mathbf{E}}_{\mathrm{t}}^{(k)}, \mathbf{e}_q^{(k)} \rangle = \langle \widehat{\mathbf{E}}_{\mathrm{t}}^{(k)}, \mathbf{e}_q^{(k)} \rangle \quad \forall q = 1 ... N_{\mathrm{m}}^{(k)} \\ \langle \widetilde{\mathbf{H}}_{\mathrm{t}}^{(k)}, \mathbf{h}_q^{(k)} \rangle = \langle \widehat{\mathbf{H}}_{\mathrm{t}}^{(k)}, \mathbf{h}_q^{(k)} \rangle \quad \forall q = 1 ... N_{\mathrm{m}}^{(k)}. \end{cases} \tag{22}$$

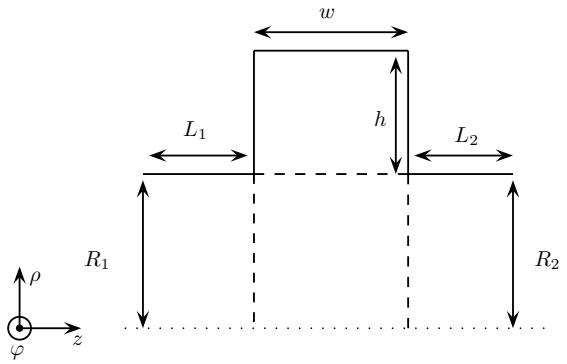

Fig. 4. Longitudinal section of a circular waveguide stub. The dashed lines identify the four patches that are used to describe the geometry. The dotted line is the waveguide axis.

The fields $\widehat{\mathbf{E}}_{\mathrm{t}}^{(k)}$ and $\widehat{\mathbf{H}}_{\mathrm{t}}^{(k)}$ are represented in terms of modes, whereas $\widetilde{\mathbf{E}}_{\mathrm{t}}^{(k)}$ and $\widetilde{\mathbf{H}}_{\mathrm{t}}^{(k)}$ in terms of MEM basis functions restricted to the access ports. By recalling (1)-(2), (22) can be re-written as:

$$\begin{cases} \mathbf{T}_k^{(\mathrm{e,e})} \cdot \mathbf{c}^{(\mathrm{e})} + \mathbf{T}_k^{(\mathrm{e,h})} \cdot \mathbf{c}^{(\mathrm{h})} = \widehat{\mathbf{V}}^{(k)} \\ \mathbf{T}_k^{(\mathrm{h,e})} \cdot \mathbf{c}^{(\mathrm{e})} + \mathbf{T}_k^{(\mathrm{h,h})} \cdot \mathbf{c}^{(\mathrm{h})} = \widehat{\mathbf{I}}^{(k)}, \end{cases} \tag{23}$$

where the matrices $\mathbf{T}_k^{(\cdot,\cdot)}$ contain the projections of the MEM basis function on the modes of the k-th waveguide.

The solution of the hybrid equivalent circuit yields the expression of the modal voltage and current vectors $\widehat{\mathbf{V}}^{(k)}$ and $\widehat{\mathbf{I}}^{(k)}$ in terms of the modal generators $\mathring{\mathbf{i}}^{(k)}$ and $\mathring{\mathbf{v}}^{(k)}$ and of the modal incidence $\mathbf{V}^{(k,\mathrm{inc})}$. These relationships are:

$$\begin{aligned} \widehat{\mathbf{V}}^{(1)} &= \mathbf{V}^{(1,\mathrm{inc})} - \frac{1}{2}\mathbf{Z}_\infty^{(1)} \cdot \mathring{\mathbf{i}}^{(1)} + \frac{1}{2}\mathring{\mathbf{v}}^{(1)} \\ \widehat{\mathbf{I}}^{(1)} &= \mathbf{Y}_\infty^{(1)} \cdot \mathbf{V}^{(1,\mathrm{inc})} + \frac{1}{2}\mathring{\mathbf{i}}^{(1)} - \frac{1}{2}\mathbf{Y}_\infty^{(1)} \cdot \mathring{\mathbf{v}}^{(1)} \\ \widehat{\mathbf{V}}^{(2)} &= \mathbf{V}^{(2,\mathrm{inc})} + \frac{1}{2}\mathbf{Z}_\infty^{(2)} \cdot \mathring{\mathbf{i}}^{(2)} + \frac{1}{2}\mathring{\mathbf{v}}^{(2)} \\ \widehat{\mathbf{I}}^{(2)} &= -\mathbf{Y}_\infty^{(2)} \cdot \mathbf{V}^{(2,\mathrm{inc})} + \frac{1}{2}\mathring{\mathbf{i}}^{(2)} + \frac{1}{2}\mathbf{Y}_\infty^{(2)} \cdot \mathring{\mathbf{v}}^{(2)}, \end{aligned} \tag{24}$$

where $\mathbf{Z}_\infty^{(k)}$ and $\mathbf{Y}_\infty^{(k)}$ are the diagonal matrices containing the modal characteristic impedances and admittances in the k-th waveguide. By substituting (24) in (23), the following linear system is derived:

$$\mathbf{T} \cdot \mathbf{c} = \mathbf{D} \cdot \mathbf{x} + \mathbf{K} \cdot \mathbf{V}^{(\mathrm{inc})}. \tag{25}$$

Appendix A reports the expressions for matrices $\mathbf{T}$, $\mathbf{D}$ and $\mathbf{K}$ for the two-port circular waveguide structure of Fig. 2. The substitution of (21) into (25) yields:

$$\mathbf{x} = [\mathbf{T} \cdot \mathbf{G} - \mathbf{D}]^{-1} \cdot \mathbf{K} \cdot \mathbf{V}^{(\mathrm{inc})}.$$

This formula provides the unknown modal generators in terms of the incident fields at the access ports. At this point, it is straightforward both to derive the expression of the generalized scattering matrix $\mathbf{S}$ of the device and to evaluate the fields inside the structure by (21).

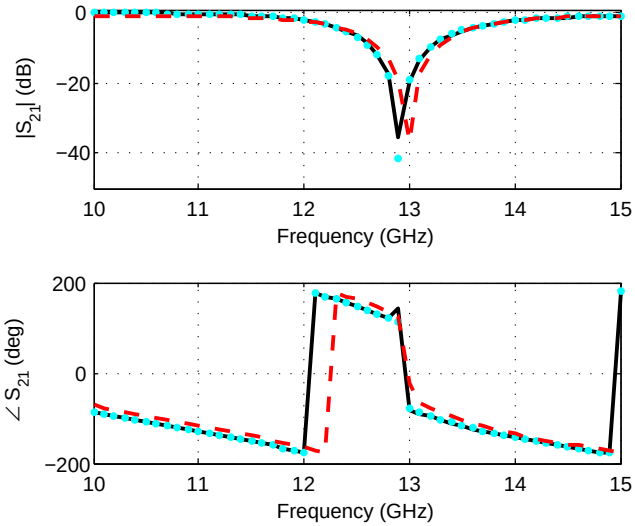

Fig. 5. Magnitude and phase of the transmission coefficient S_{21} of the circular waveguide stub shown in Fig. 4 ($R_1 = R_2 = 9.525$ mm, $h = 5$ mm, $w = 6$ mm, $L_1 = L_2 = 4$ mm). The dotted curve (reference) refers to the MMT simulation. The solid and dashed curves are obtained by the MEM, using singular and polynomial basis functions, respectively.

III. Results

In this section a validation of the mortar-element method (MEM) is presented by considering two simple benchmark cases and a more complex axisymmetric waveguide structure used in horn antennas, *i.e.*, a choked mode converter.

A. Circular waveguide stub

As a first benchmark case, the Ku-band circular waveguide stub shown in Fig. 4 is considered. The input and output waveguide radii are $R_1 = R_2 = 9.525$ mm, the stub width is $w = 6$ mm, the stub length is $h = 5$ mm and the lengths of the input lines are $L_1 = L_2 = 4$ mm. The electromagnetic field at the access ports is represented by using $N_{\rm m}^{(1)} = N_{\rm m}^{(2)} = N_{\rm m}^{(\rm MEM)} = 10$ modes, whereas the unknowns E_φ and H_φ are expanded with $N_{\rm fun}^{(\rm e)}$ and $N_{\rm fun}^{(\rm h)}$ global basis functions, respectively. Although the polynomial degree of the basis functions $\{u_c^{(\rm e)}\}$ and $\{u_c^{(\rm h)}\}$ is the same, $N_{\rm fun}^{(\rm e)}$ is generally smaller due to the enforcement of the essential boundary condition. The reference solution is obtained by a mode-matching code. In order to ensure the convergence of the scattering parameters, $N_{\rm m}^{(\rm MMT)} = 20$ modes are used at the step aperture. Fig. 5 reports the comparison between the MEM and MMT curves relative to the transmission coefficient S_{21} of the $\rm TE_{11}$ mode. The dashed curve is obtained by the MEM, using $N_{\rm fun}^{(\rm e)} = 49$ and $N_{\rm fun}^{(\rm h)} = 70$ polynomial basis functions. As discussed previously in Subsection II-B the field singularity at the sharp edges is better modeled by basis functions augmented with weights, which keep into account the asymptotic behavior of the field in the proximity of the edges. The solid curve of Fig. 5 refers to the MEM with $N_{\rm fun}^{(\rm e)} = 32$ and $N_{\rm fun}^{(\rm h)} = 46$ weighted basis functions (generated by means of sixth-order polynomials). The gain in accuracy provided by the singular basis functions is clearly visible, with particular reference to the frequency of the transmission zero.

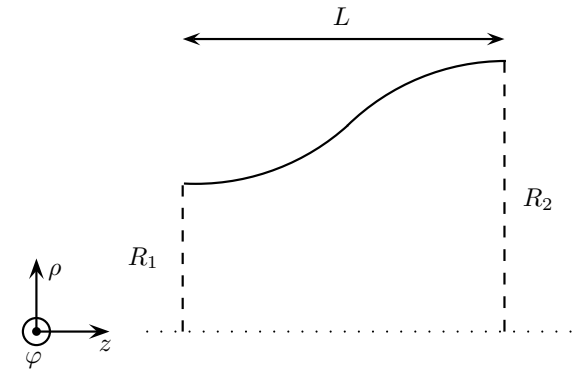

Fig. 6. Longitudinal section of the smooth waveguide transition considered as a second benchmark case. This structure is described with a single patch. The dashed lines denote the access waveguide ports with input waveguide radii R_1 and R_2; L is the length of the structure.

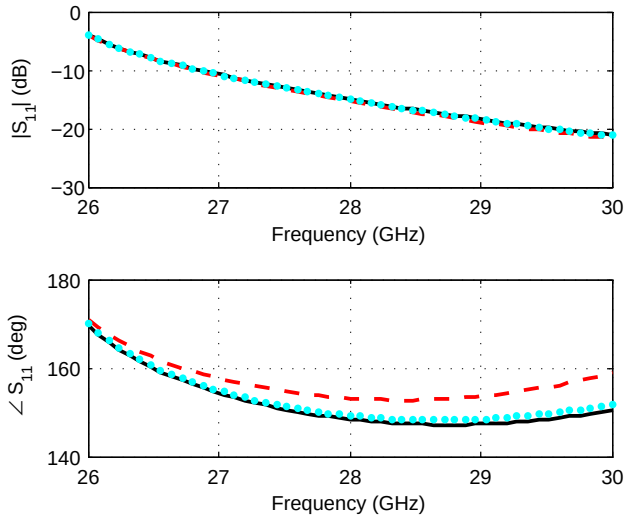

Fig. 7. Reflection coefficient S_{11} of the smooth waveguide transition shown in Fig. 6 ($R_1 = 3.4$ mm, $R_2 = 5$ mm, $L = 4$ mm). The solid curve refers to the MEM simulations, whereas the dashed and dotted lines indicate the MMT results for the discretizations $\lambda_{\rm min}/20$ and $\lambda_{\rm min}/100$, respectively.

B. Smooth waveguide transition

The Ka-band smooth waveguide transition shown in Fig. 6 is considered as a second benchmark case. This structure is relevant in order to assess the capability of the method to describe structures with curved sides by using a single patch. The input and output waveguide radii are $R_1 = 3.4$ mm and $R_2 = 5$ mm, and the length of the junction is $L = 4$ mm. The electromagnetic fields at the access ports are represented by using $N_{\rm m}^{(\rm MEM)} = 10$ modes, whereas E_φ and H_φ are expanded with $N_{\rm fun}^{(\rm e)} = 56$ and $N_{\rm fun}^{(\rm h)} = 64$ global basis functions (generated by means of eighth-order polynomials), respectively.

The reference solution is obtained by a staircase approximation of the profile that is analyzed as a cascade of circular

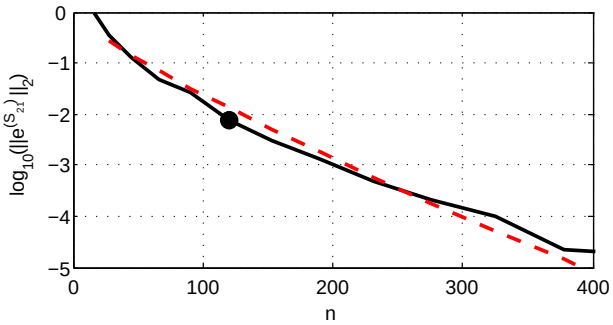

Fig. 8. Convergence analysis of the MEM applied to the smooth waveguide transition shown in Fig. 6 ($R_1 = 3.4$ mm, $R_2 = 5$ mm, $L = 4$ mm). The solid curve report the 2-norm relative error $||e^{(S_{11})}||_2$ in the reflection coefficient versus the total number of entire domain basis functions $n = N_{\rm fun}^{(\rm e)} + N_{\rm fun}^{(\rm h)}$ (non-weighted polynomials). The dot refers to the MEM simulation shown in Fig. 7, whereas the dashed line indicates the exponential behaviour $\propto n^{0.8}$

waveguide steps, each one simulated by the MMT. To assess the MMT accuracy, two discretizations are considered, *i.e.*, $\lambda_{\rm min}/20$ (8 steps) and $\lambda_{\rm min}/100$ (40 steps) [4]. $N_{\rm m}^{(\rm MMT)} = 20$ modes are used in the computation of the GSM of each step. The comparison between the reflection coefficient at port 1 for the $\rm TE_{11}$ mode computed by the MEM and MMT is reported in Fig. 7. It can be noticed that if a high accuracy is required also in the evaluation of the phase of the reflection coefficient, a very small discretization distance ($d_{\rm min} = \lambda_{\rm min}/100$) should be used for the MMT. In this situation, the computation time would be approximately 10 times higher than the MEM one.

A convergence study of the MEM with respect to the number of basis functions used to represent E_φ and H_φ has been carried out for this structure. In this case, owing to the absence of sharp edges, polynomials can properly represent the electromagnetic field and, hence, the use of polynomials with weighting functions is not investigated. Figure 8 shows the 2-norm relative error $||e^{(S_{11})}||_2$ in the reflection coefficient versus the total number of entire domain basis functions $n = N_{\rm fun}^{(\rm e)} + N_{\rm fun}^{(\rm h)}$. The dot refers to the MEM simulation shown in Fig. 7 for which an accuracy better than 1% is achieved. An exponentially-convergent behavior $\propto n^r$, typical of spectral methods, is observed with an exponential index of convergence r of about 0.8 (dashed line in Fig. 8).

C. Choked mode converter

The MEM has been applied also to the analysis of a choked mode converter [5]. This device is used as the input section of corrugated horn antennas [6], [7], in order to transform the $\rm TE_{11}$ mode into the balanced hybrid $\rm HE_{11}$ mode. Along with very low values of side-lobe level and cross-polarization, this mode converter provides significant advantages in terms of manufacturing. A 3-D cut of the choked mode converter of the feed horn described in [7] operating in the X-band is drawn in Fig. 9. The entire feed horn can be efficiently analyzed with a hybrid MEM-MMT, where mode-matching is conveniently used to analyze the vertical corrugated section.

Figure 10 shows the comparisons between the values of the $\rm TE_{11}$-$\rm TE_{11}$ reflection coefficient computed with the MEM

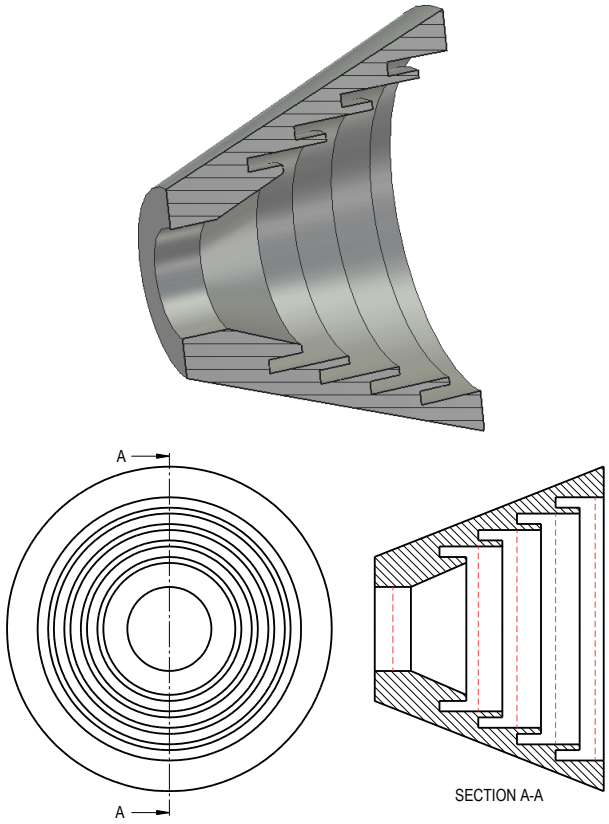

Fig. 9. Choked mode converter described in [7]. In the longitudinal section, the dashed lines indicate the reference planes of the building blocks analyzed in the MEM simulation.

and the frequency domain solver of CST Microwave Studio. In the MEM analysis, the structure has been decomposed into the four blocks shown in the longitudinal section displayed in Fig. 9. For each of them, the GSM has been evaluated by using $N_{\rm m}^{(\rm MEM)} = 15$, $N_{\rm fun}^{(\rm e)} = 181$ and $N_{\rm fun}^{(\rm h)} = 216$ generated by means of ninth-order polynomials). Finally, the GSM of the entire structure has been computed as the cascade of the four blocks. A remarkable agreement between the two methods has been achieved, thus validating the applicability of the MEM to the analysis of complex axisymmetric waveguide devices.

The $\rm TE_{11}$ to $\rm HE_{11}$ mode conversion efficiency $\eta_{\rm conv}$ of the choked mode converter is shown in Fig. 11 (top). As well known, this parameter is correlated to the maximum cross-polarization component of the radiated field, shown in the lower diagram of Fig. 11. The $[0°, 60°]$ angular range and the third Ludwig definition have been considered in the evaluation of the cross-polarization curve. For this computation, the aperture field distribution has been obtained by connecting the GSM of the choked mode converter to the multi-modal load corresponding to the junction between a (flanged) circular waveguide and free-space. The GSM of the choked mode converter has been computed with the present technique, whereas the multi-modal load has been obtained with an in-house MoM code.

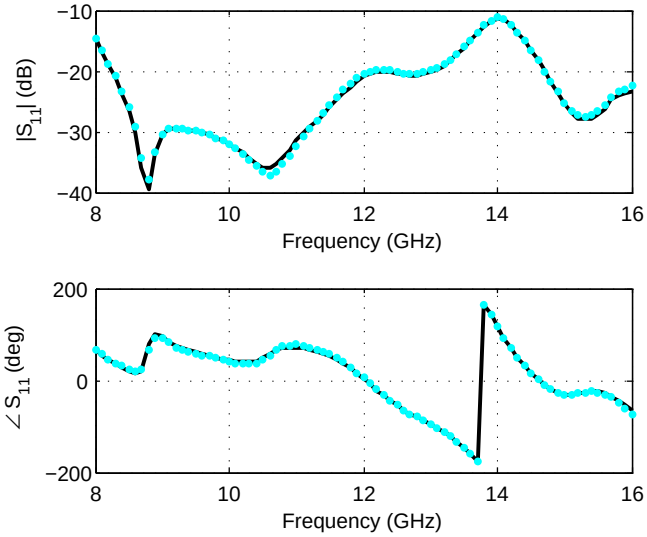

Fig. 10. Reflection coefficient for the TE_{11} mode of the choked mode converter shown in Fig. 9. The solid and dotted curves refer to results obtained with the MEM and the frequency domain solver of CST Microwave Studio, respectively.

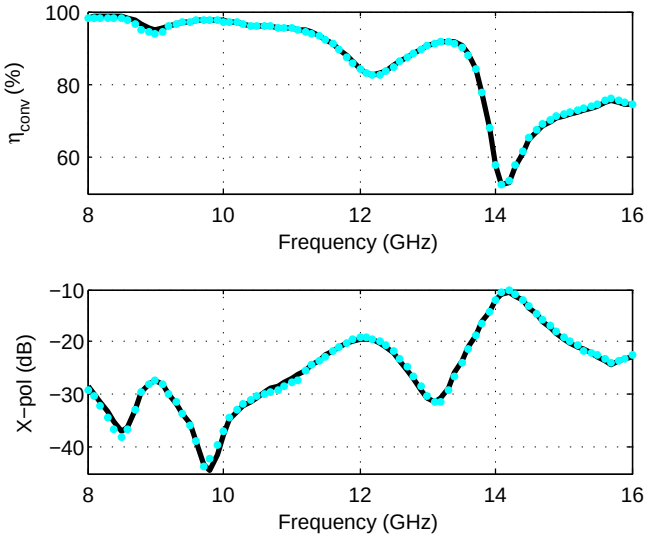

Fig. 11. Modal conversion characteristics of the choked mode converter shown in Fig. 9. Top: TE_{11} to HE_{11} mode conversion efficiency η_{conv}. Bottom: maximum cross-polar component of the radiated field in the $[0°, 60°]$ angular range. The solid and dotted curves refer to the results obtained with the MEM and the frequency-domain solver of CST Microwave Studio.

IV. Conclusion

In this paper, a novel analysis technique of axisymmetric guiding structures has been presented. The main advantage of the present method is its capability of efficiently analyzing any structure, including tapered transitions without profile approximation, with any type of waveguides at the access ports, *e.g.*, circular, coaxial or conical waveguides. The results obtained with the code implementing this scheme have been compared to reference solutions for two benchmark cases and for a choked mode converter, finding a very good agreement.

Appendix A
Expressions of the Matrix Elements

This appendix reports the expressions of the matrix elements introduced in Section II for the two-port circular waveguide structure shown in Fig. 2. The matrix $\mathbf{A}$ in (19) is defined as:

$$\mathbf{A} = \begin{bmatrix} \mathbf{A}^{(\mathrm{e,e})} & \mathbf{A}^{(\mathrm{e,h})} \\ \mathbf{A}^{(\mathrm{h,e})} & \mathbf{A}^{(\mathrm{h,h})} \end{bmatrix},$$

where:

$$\begin{aligned}(\mathbf{A}^{(\mathrm{e,e})})_{rc} =& \mathrm{j}k_0 Y_0 \left\{ \iint_\Omega u_c^{(\mathrm{e})} v_r^{(\mathrm{e})*} \,\mathrm{d}z\,\mathrm{d}\rho + \right. \\ &+ \iint_\Omega \frac{\rho^2}{m^2 - k_0^2\rho^2} \frac{\partial u_c^{(\mathrm{e})}}{\partial z} \frac{\partial v_r^{(\mathrm{e})*}}{\partial z} \,\mathrm{d}z\,\mathrm{d}\rho + \\ &+ \iint_\Omega \frac{\rho^2}{m^2 - k_0^2\rho^2} \frac{\partial u_c^{(\mathrm{e})}}{\partial \rho} \frac{\partial v_r^{(\mathrm{e})*}}{\partial \rho} \,\mathrm{d}z\,\mathrm{d}\rho + \\ &\left. + \iint_\Omega \frac{\rho}{m^2 - k_0^2\rho^2} u_c^{(\mathrm{e})} \frac{\partial v_r^{(\mathrm{e})*}}{\partial \rho} \,\mathrm{d}z\,\mathrm{d}\rho \right\}\end{aligned}$$

$$\begin{aligned}(\mathbf{A}^{(\mathrm{e,h})})_{rc} =& \mathrm{j}m \left\{ - \iint_\Omega \frac{\rho}{m^2 - k_0^2\rho^2} \frac{\partial u_c^{(\mathrm{h})}}{\partial z} \frac{\partial v_r^{(\mathrm{e})*}}{\partial \rho} \,\mathrm{d}z\,\mathrm{d}\rho + \right. \\ &\left. + \iint_\Omega \frac{1}{m^2 - k_0^2\rho^2} \frac{\partial (\rho u_c^{(\mathrm{h})})}{\partial \rho} \frac{\partial v_r^{(\mathrm{e})*}}{\partial z} \,\mathrm{d}z\,\mathrm{d}\rho \right\}\end{aligned}$$

$$\begin{aligned}(\mathbf{A}^{(\mathrm{h,e})})_{rc} =& \mathrm{j}m \left\{ - \iint_\Omega \frac{\rho}{m^2 - k_0^2\rho^2} \frac{\partial u_c^{(\mathrm{e})}}{\partial z} \frac{\partial v_r^{(\mathrm{h})*}}{\partial \rho} \,\mathrm{d}z\,\mathrm{d}\rho + \right. \\ &\left. + \iint_\Omega \frac{1}{m^2 - k_0^2\rho^2} \frac{\partial (\rho u_c^{(\mathrm{e})})}{\partial \rho} \frac{\partial v_r^{(\mathrm{h})*}}{\partial z} \,\mathrm{d}z\,\mathrm{d}\rho \right\}\end{aligned}$$

$$\begin{aligned}(\mathbf{A}^{(\mathrm{h,h})})_{rc} =& -\mathrm{j}k_0 Z_0 \left\{ \iint_\Omega u_c^{(\mathrm{h})} v_r^{(\mathrm{h})*} \,\mathrm{d}z\,\mathrm{d}\rho + \right. \\ &+ \iint_\Omega \frac{\rho^2}{m^2 - k_0^2\rho^2} \frac{\partial u_c^{(\mathrm{h})}}{\partial z} \frac{\partial v_r^{(\mathrm{h})*}}{\partial z} \,\mathrm{d}z\,\mathrm{d}\rho + \\ &+ \iint_\Omega \frac{\rho^2}{m^2 - k_0^2\rho^2} \frac{\partial u_c^{(\mathrm{h})}}{\partial \rho} \frac{\partial v_r^{(\mathrm{h})*}}{\partial \rho} \,\mathrm{d}z\,\mathrm{d}\rho + \\ &\left. + \iint_\Omega \frac{\rho}{m^2 - k_0^2\rho^2} u_c^{(\mathrm{h})} \frac{\partial v_r^{(\mathrm{h})*}}{\partial \rho} \,\mathrm{d}z\,\mathrm{d}\rho \right\}.\end{aligned}$$

The matrix $\mathbf{B}$ is defined as:

$$\mathbf{B} = \begin{bmatrix} -\mathbf{B}^{(\mathrm{e},1)} & \mathbf{0} & \mathbf{B}^{(\mathrm{e},2)} & \mathbf{0} \\ \mathbf{0} & -\mathbf{B}^{(\mathrm{h},1)} & \mathbf{0} & \mathbf{B}^{(\mathrm{h},2)} \end{bmatrix},$$

where, for each k-th port:

$$(\mathbf{B}^{(\mathrm{e},k)})_{rn} = \int_0^{\rho_{\mathrm{wg}}^{(k)}} h_{\rho,n}^{(k)} v_r^{(\mathrm{e})*} \,\mathrm{d}\rho$$

$$(\mathbf{B}^{(\mathrm{h},k)})_{rn} = \int_0^{\rho_{\mathrm{wg}}^{(k)}} e_{\rho,n}^{(k)} v_r^{(\mathrm{h})*} \,\mathrm{d}\rho,$$

and $h^{(k)}_{\rho,n}$, $e^{(k)}_{\rho,n}$ are the ρ components of the magnetic and electric n-th mode functions.

As for (25), associated to the continuity conditions at the waveguide ports, the matrix $\mathbf{T}$ containing the projections of the MEM basis functions on the waveguide modes is:

$$\mathbf{T} = \begin{bmatrix} \mathbf{T}_1^{(\mathrm{e},\mathrm{e})} & \mathbf{T}_1^{(\mathrm{e},\mathrm{h})} \\ \mathbf{T}_1^{(\mathrm{h},\mathrm{e})} & \mathbf{T}_1^{(\mathrm{h},\mathrm{h})} \\ \mathbf{T}_2^{(\mathrm{e},\mathrm{e})} & \mathbf{T}_2^{(\mathrm{e},\mathrm{h})} \\ \mathbf{T}_2^{(\mathrm{h},\mathrm{e})} & \mathbf{T}_2^{(\mathrm{h},\mathrm{h})} \end{bmatrix},$$

where:

$$\begin{aligned}
(\mathbf{T}_k^{(\mathrm{e},\mathrm{e})})_{rc} &= \int_0^{\rho_{\mathrm{wg}}^{(k)}} u_c^{(\mathrm{e})} e_{\varphi,r}^{(k)*} \rho \,\mathrm{d}\rho + \\
&\quad - \mathrm{j}m \int_0^{\rho_{\mathrm{wg}}^{(k)}} \frac{1}{m^2 - k_0^2\rho^2} \frac{\partial(\rho u_c^{(\mathrm{e})})}{\partial \rho} e_{\rho,r}^{(k)*} \rho \,\mathrm{d}\rho \\
(\mathbf{T}_k^{(\mathrm{e},\mathrm{h})})_{rc} &= -\mathrm{j}k_0 Z_0 \int_0^{\rho_{\mathrm{wg}}^{(k)}} \frac{\rho^2}{m^2 - k_0^2\rho^2} \frac{\partial u_c^{(\mathrm{e})}}{\partial z} e_{\rho,r}^{(k)*} \rho \,\mathrm{d}\rho \\
(\mathbf{T}_k^{(\mathrm{h},\mathrm{h})})_{rc} &= \int_0^{\rho_{\mathrm{wg}}^{(k)}} u_c^{(\mathrm{h})} h_{\varphi,r}^{(k)*} \rho \,\mathrm{d}\rho + \\
&\quad - \mathrm{j}m \int_0^{\rho_{\mathrm{wg}}^{(k)}} \frac{1}{m^2 - k_0^2\rho^2} \frac{\partial(\rho u_c^{(\mathrm{h})})}{\partial \rho} h_{\rho,r}^{(k)*} \rho \,\mathrm{d}\rho \\
(\mathbf{T}_k^{(\mathrm{h},\mathrm{e})})_{rc} &= \mathrm{j}k_0 Y_0 \int_0^{\rho_{\mathrm{wg}}^{(k)}} \frac{\rho^2}{m^2 - k_0^2\rho^2} \frac{\partial u_c^{(\mathrm{h})}}{\partial z} h_{\rho,r}^{(k)*} \rho \,\mathrm{d}\rho.
\end{aligned}$$

The matrix $\mathbf{D}$, derived from the modal circuit of Fig. 3 is:

$$\mathbf{D} = \begin{bmatrix} -\frac{1}{2}\mathbf{Z}_\infty^{(1)} & \frac{1}{2}\mathbf{I} & \mathbf{0} & \mathbf{0} \\ \frac{1}{2}\mathbf{I} & -\frac{1}{2}\mathbf{Y}_\infty^{(1)} & \mathbf{0} & \mathbf{0} \\ \mathbf{0} & \mathbf{0} & \frac{1}{2}\mathbf{Z}_\infty^{(2)} & \frac{1}{2}\mathbf{I} \\ \mathbf{0} & \mathbf{0} & \frac{1}{2}\mathbf{I} & \frac{1}{2}\mathbf{Y}_\infty^{(2)} \end{bmatrix},$$

where $\mathbf{I}$ is the identity matrix, $\mathbf{Z}_\infty^{(k)}$ and $\mathbf{Y}_\infty^{(k)}$ are the diagonal matrices with the modal impedances and admittances at the k-th access port. Similarly, the matrix $\mathbf{K}$ is:

$$\mathbf{K} = \begin{bmatrix} \mathbf{I} & \mathbf{0} \\ \mathbf{Y}_\infty & \mathbf{0} \\ \mathbf{0} & \mathbf{I} \\ \mathbf{0} & -\mathbf{Y}_\infty^{(2)} \end{bmatrix}.$$

Appendix B
Calculation of the singular integrals

The calculation of the elements of the matrix $\mathbf{A}$ in (19) requires the evaluation of integrals of the form:

$$\iint_{\Omega_i} \frac{f(z,\rho)}{m^2 - k_0^2\rho^2} \,\mathrm{d}\rho \,\mathrm{d}z, \tag{26}$$

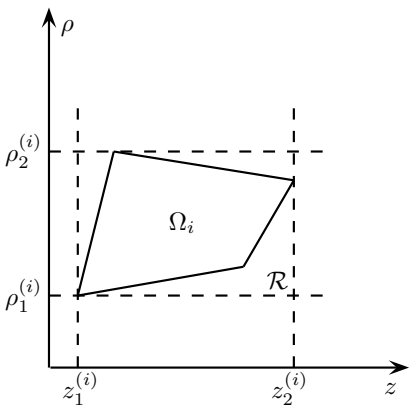

Fig. 12. Example of integration domain Ω_i enclosed by the rectangle $\mathcal{R}$ for the application of the singularity-subtraction scheme. The rectangle $\mathcal{R}$ has width R and length L.

where the function $f(z,\rho)$ is the product of the basis functions and of their derivatives and Ω_i is the patch domain (see Fig. 12 where the example of a quadrilateral patch is shown). The integrand function is singular in $\rho = \pm m/k_0$, but the pole $\rho = -m/k_0$ clearly never falls in the integration domain. On the contrary, depending on the patch geometry and on the frequency, the pole $\rho = m/k_0$ can belong to Ω_i and its presence has to be taken into account for the correct and efficient evaluation of (26). In this case, a subtraction scheme is exploited:

$$\begin{aligned}
&\iint_{\Omega_i} \frac{f(z,\rho)}{m^2 - k_0^2\rho^2} \mathrm{d}\rho \,\mathrm{d}z = \iint_{\Omega_i} \frac{g(z,\rho)}{m - k_0\rho} \mathrm{d}\rho \,\mathrm{d}z = \\
&\iint_{\Omega_i} \frac{g(z,\rho) - g(z,m/k_0)}{m - k_0\rho} \mathrm{d}\rho \mathrm{d}z + \iint_{\Omega_i} \frac{g(z,m/k_0)}{m - k_0\rho} \mathrm{d}\rho \,\mathrm{d}z,
\end{aligned} \tag{27}$$

where $g(z,\rho) = f(z,\rho)/(m + k_0\rho)$ is a smooth function in Ω_i. The first term in the right side of (27) is regular and can be computed in the parent domain (u,v), where the basis functions are defined, by means of the Gauss-Legendre quadrature rule. The second term contains the singular part and its computation requires an analytical algebraic manipulation. First, let $\mathcal{R} = [z_1^{(i)}, z_2^{(i)}] \times [\rho_1^{(i)}, \rho_2^{(i)}]$ be the smallest rectangle in the (z,ρ) domain that contains the integration domain Ω_i (see Fig. 12). Then,

$$\begin{aligned}
&\iint_{\Omega_i} \frac{g(z,m/k_0)}{m - k_0\rho} \mathrm{d}\rho \,\mathrm{d}z = \\
&\iint_{\mathcal{R}} \frac{g(z,m/k_0)\chi_{\Omega_i}(z,\rho)}{m - k_0\rho} \mathrm{d}\rho \,\mathrm{d}z = \\
&-\frac{1}{k_0} \int_{z_1^{(i)}}^{z_2^{(i)}} g(z,m/k_0) \left[\int_{\rho_1^{(i)}}^{\rho_2^{(i)}} \frac{\chi_{\Omega_i}(z,\rho)}{\rho - m/k_0} \,\mathrm{d}\rho \right] \mathrm{d}z,
\end{aligned} \tag{28}$$

where $\chi_{\Omega_i}(z,\rho)$ is the characteristic function of the domain Ω_i. The inner integral can be computed analytically as the limit of the infinitesimal losses case:

$$\int_{\rho_1^{(i)}}^{\rho_2^{(i)}} \frac{\chi_{\Omega_i}(z,\rho)}{\rho - m/k_0} \mathrm{d}\rho = \mathrm{j}\pi\chi_{\Omega_i}(z,m/k_0) + \log\left|\frac{\rho_{\mathrm{M}}(z) - m/k_0}{\rho_{\mathrm{m}}(z) - m/k_0}\right|,$$

TABLE I
CONVERGENCE STUDY OF THE INTEGRATION SCHEME.

N_{quad}	$e^{(A_{rt}^{(\mathrm{e,e})})}$
4	1
8	10^{-1}
16	10^{-6}
32	10^{-12}
64	10^{-12}

where $\rho_{\mathrm{m}}(z)$ and $\rho_{\mathrm{M}}(z)$ are the minimum and maximum ρ coordinates of Ω_i corresponding to the longitudinal coordinate z; their expressions as a function of z are analytical. Inserting the previous formula in (28) yields

$$\begin{aligned}\iint_{\Omega_i} \frac{g(z,m/k_0)}{m-k_0\rho}\mathrm{d}\rho\,\mathrm{d}z = \\ -\frac{\mathrm{j}\pi}{k_0}\int_{z_1^{(i)}}^{z_2^{(i)}} g(z,m/k_0)\chi_{\Omega_i}(z,m/k_0)\,\mathrm{d}z + \\ -\frac{1}{k_0}\int_{z_1^{(i)}}^{z_2^{(i)}} g(z,m/k_0)\log|\rho_{\mathrm{M}}(z)-m/k_0|\,\mathrm{d}z + \\ +\frac{1}{k_0}\int_{z_1^{(i)}}^{z_2^{(i)}} g(z,m/k_0)\log|\rho_{\mathrm{m}}(z)-m/k_0|\,\mathrm{d}z.\end{aligned}$$

Since the function in the first integral is regular, then a Gauss-Legendre quadrature rule scheme is applied. The second and third integrand functions exhibit a logarithmic singularity in $z = z_0$ that can slow down the convergence of the numerical scheme. For their computation a change of variables of the type $z = z_0 + \mathrm{e}^{\mp t}$ is applied. In this way, the new integral function is regular and can be efficiently computed exploiting a Gauss-Laguerre quadrature scheme. The line integrals involved in the calculation of the elements of the matrix $\mathbf{T}$ are carried out using a similar numerical scheme. In Table I a convergence study of the present integration scheme is reported as a function of the number of nodes N_{quad} used both in the Gauss-Legendre and Gauss-Laguerre quadrature schemes. The study refers to the matrix element $(\mathbf{A}^{(\mathrm{e,e})})_{rc}$ with the indexes r and t corresponding to the higher-order basis function that is defined on the single patch of the smooth waveguide transition of Fig. 6. The frequency is set so that $\rho = m/k_0 = R_1/2$.

REFERENCES

[1] L. Zappelli, "On the definition of the generalized scattering matrix of a lossless radial line," *IEEE Trans. Microw. Theory Techn.,* vol. 52, no. 6, pp. 1654-1662, June 2004.

[2] G. Addamo, O. A. Peverini, G. Virone, R. Tascone and R. Orta, "Model-order reduction technique for the efficient analysis of complex waveguide structures - an application to the design of corrugated horns," *IEEE Antennas Wireless Propag. Lett.,* vol. 59, no. 7, pp. 1685-1695, July 2011.

[3] A. K. Bhattacharyya, "Multimode moment method formulation for waveguide discontinuities," *IEEE Trans. Microw. Theory Techn.,* vol. 42, no. 8, pp. 1567-1571 Aug. 1994.

[4] K. K. Chan and S. K. Rao, "Design of high efficiency circular horn feeds for multibeam reflector applications," *IEEE Trans. Antennas Propag.,* vol. 56, no. 1, pp. 253-258, Jan. 2008.

[5] J. Teniente Vallinas, "Modern corrugated horn antennas," Ph. D. Thesis, Universidad Pública de Navarra, Pamplona, Spain, July 2003.

[6] J. Teniente Vallinas, D. Goñi, R. Gonzalo and C. del-Río, "Choked gaussian antenna: extremely low sidelobe compact antenna design," *IEEE Antennas Propag. Lett.,* vol. 1, no. 1, pp. 200-202, 2002.

[7] J. Teniente Vallinas, R. Gonzalo and C. del-Río, "Reply to "Comments on 'Choked gaussian antenna: extremely low sidelobe compact antenna design'"," *IEEE Antennas Propag. Lett.,* vol. 2, no. 1, pp. 364-366, 2003.

[8] M. A. Morgan and K. K. Mei, "Finite-element computation of scattering by inhomogeneous penetrable bodies of revolution," *IEEE Trans. Antennas Propag.,* vol. 27, no. 2, pp. 202-214, Mar. 1979.

[9] J. M. Gil, J. Monge, J. Rubio, and J. Zapata, "A CAD-oriented method to analyze and design radiating structures based on bodies of revolution by using finite elements and generalized scattering matrix," *IEEE Trans. Antennas Propag.,* vol. 54, no. 3, pp. 899-907, Mar. 2006.

[10] U. Lee, "Spectral element method in structural dynamics," John Wiley & Sons (Asia), Singapore.

[11] C. Canuto, M. Y. Hussaini, A. Quarteroni and T. A. Zang, "Spectral methods in fluid dynamics," Berlin, Germany: Springer-Verlag, 1988.

[12] C. Canuto, M. Y. Hussaini, A. Quarteroni and T. A. Zang, "Spectral methods: evolution to complex geometries and applications to fluid dynamics," Berlin, Germany: Springer-Verlag, 2007.

[13] J. H. Lee, T. Xiao and Q. H. Liu, "A 3-D spectral-element method using mixed-order curl conforming vector basis functions for electromagnetics fields," *IEEE Trans. Microw. Theory Techn.,* vol. 54, no. 1, pp. 437-444, Jan. 2006.

[14] Y. Liu, J. H. Lee, T. Xiao and Q. H. Liu, "A spectral-element time-domain solution of Maxwell's equations," *Microw. Opt. Technol. Lett.,* vol. 48, no. 4, pp. 673-680, Apr. 2006.

[15] J. H. Lee and Q. H. Liu, "A 3-D spectral-element time-domain method for electromagnetic simulation," *IEEE Trans. Microw. Theory Techn.,* vol. 55, no. 5, pp. 983-991, May 2007.

[16] O. A. Peverini, G. Addamo, G. Virone, R. Tascone and R. Orta, "A spectral-element method for the analysis of 2-D waveguide devices with sharp edges and irregular shapes," *IEEE Trans. Microw. Theory Techn.,* vol. 59, no. 7, pp. 1685-1695 July 2011.

[17] L. B. Felsen and N. Marcuvitz, "Radiation and scattering of waves," John Wiley & Sons, Jan. 1994.

[18] J. Meixner, "The behavior of electromagnetic fields at edges," *IEEE Trans. Antennas Propag.*. vol. 20, no. 4, pp. 442-446, July 1972.

[19] P. P. Silvester and R. L. Ferrari, "Finite elements for electrical engineers," Cambridge University Press, Cambridge, 1996.

Alberto Tibaldi (M'12) was born in Casale Monferrato, Italy, on February 21, 1987. In July 2009 and in November 2011 he received the B.Sc. and M.Sc degrees in Electronic Engineering (*summa cum laude*) from the Politecnico di Torino. In 2012 he joins the Applied Electromagnetics and Electronic Devices Group of the Istituto di Elettronica e di Ingegneria dell'Informazione e delle Telecomunicazioni (IEIIT) of the Consiglio Nazionale delle Ricerche (CNR) as Ph.D. student. From June to December 2013 he was a visiting member of the Terahertz Sensing Group, Delft University of Technology, Delft, The Netherlands. His scientific interests mainly regard the numerical simulation of electromagnetic passive devices.

Giuseppe Addamo was born in Messina, Italy, in 1979. He received the Laurea degree (*summa cum laude*) in electronic engineering and Ph.D. degree in electronic and communication engineering from the Politecnico di Torino, Turin, Italy, in 2003 and 2007, respectively. In January 2007, he joined the Instituto di Elettronica e di Ingegneria dell'Informazione e delle Telecomunicazioni (IEIIT), Consiglio Nazionale delle Ricerche (CNR), Turin, Italy, as a Research Fellow, and in 2012, became a Researcher. He holds practical classes in courses on electromagnetic field theory and mathematical analysis at the Politecnico di Torino. His research interests are in the areas of microwave leaky antennas, dielectric radomes, high-power feed systems (e.g., orthomode transducers (OMTs), microwave filters), corrugated horns, frequency-selective surfaces, and large dielectric radomes.

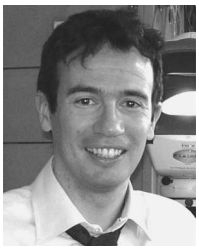

Oscar Antonio Peverini (M'12) was born in Lisbon, Portugal, in 1972. He received the Laurea degree (*summa cum laudae*) in telecommunications engineering and the Ph.D. degree in electronic and communication engineering from the Politecnico di Torino, Turin, Italy, in 1997 and 2001, respectively. From August 1999 to March 2000, he was a Visiting Member with the Applied Physics/Integrated Optics Department, University of Paderborn, Paderborn, Germany. In February 2001, he joined the Istituto di Ricerca sull'Ingegneria delle Telecomunicazioni e dell'Informazione (IRITI), Consiglio Nazionale delle Ricerche (CNR), Turin, Italy. Since December 2001, he has been a Researcher with the Istituto di Elettronica e di Ingegneria Informatica e delle Telecomunicazioni (IEIIT), CNR. He teaches courses on electromagnetic field theory and applied mathematics at the Politecnico di Torino. His research interests include modeling, design, and measurement techniques of microwave passive devices and integrated acousto-optical components for communication and scientific equipment.

Renato Orta (M'92-SM'99) received the Laurea degree in electronic engineering from the Politecnico di Torino, Turin, Italy in 1974. Since 1974, he has been a member of the Department of Electronics, Politecnico di Torino, initially as an Assistant Professor, then as an Associate Professor, and since 1999, as a Full Professor. In 1998, he was a Visiting Professor (CLUSTER Chair) with the Technical University of Eindhoven, Eindhoven, The Netherlands. He currently teaches courses on electromagnetic field theory and optical components. His research interests include the areas of microwave and optical components, radiation and scattering of electromagnetic and elastic waves, and numerical techniques.

Giuseppe Virone was born in Turin, Italy, in 1977. He received the Electronic Engineering degree (*summa cum laude*) and Ph.D. degree in electronic and communication engineering from the Politecnico di Torino, Turin, Italy, in 2001 and 2006, respectively. He is currently a Researcher with the Istituto di Elettronica e di Ingegneria Informatica e delle Telecomunicazioni (IEIIT), Consiglio Nazionale delle Ricerche (CNR), Turin, Italy. In 2002, he joined IEIIT as a Research Assistant. His research activities concern the design and numerical analysis of microwave and millimeter waveguide passive components for feed systems, antennas, frequency-selective surfaces, compensated dielectric radomes, and industrial applications.

Riccardo Tascone (M'03) was born in Genoa, Italy, in 1955. He received the Laurea degree (*summa cum laude*) in electronic engineering from the Politecnico di Torino, Turin, Italy, in 1980. From 1980 to 1982, he was with the Centro Studi e Laboratori Telecomunicazioni (CSELT), Turin, Italy, where his research mainly dealt with frequency-selective surfaces, waveguide discontinuities, and microwave antennas. In 1982, he joined the Centro Studi Propagatione e Antenne (CESPA) Consiglio Nazionale delle Ricerche (CNR), Turin, Italy, where he was initially a Researcher, and since 1991, a Senior Scientist (Dirigente di Ricerca). He has been Head of the Applied Electromagnetics Section of the Istituto di Ricerca sull'Ingeneria delle Telecomunicazioni e dell'Informazione (IRITI), an institute of CNR, Turin, Italy, and since September 2002, of the Istituto di Elettronica e di Ingegneria dell'Informazione e delle Telecomunicazioni (IEIIT), Turin, Italy, a newly established institute of CNR. He has held various teaching positions in the area of electromagnetics with the Politecnico di Torino. His current research activities are in the areas of microwave antennas, dielectric radomes, frequency-selective surfaces, radar cross section, waveguide discontinuities, microwave filters, multiplexers, optical passive devices, and radiometers for astrophysical observations.